Interfacing 2D VS_2 with Janus MoSSe: Antiferromagnetic Electric Polarization and Charge transfer Driven Half-metallicity

Dimuthu Wijethunge[1,2], Lei Zhang[1,2], Cheng Tang[1,2], Stefano Sanvito[3] and Aijun Du[1,2]*

[1]*School of Chemistry and Physics, Queensland University of Technology, Gardens Point Campus, Brisbane, QLD 4000, Australia*

[2]*Centre for Materials Science, Queensland University of Technology, Gardens Point Campus, Brisbane, QLD 4000, Australia*

[3]*School of Physics and CRANN Institute, Trinity College, Dublin 2, Ireland*

aijun.du@qut.edu.au

Abstract

Half metallic 2D materials with 100% spin polarization at the fermi level can be applied to spintronics to enhance the device efficiency. We identified that the Janus MoSSe monolayer can induce halfmetallicity in the VS_2 bilayer whose ground state magnetic order remains in an antiferromagnetic configuration. We established that half-metallicity in the bilayer VS_2 is caused by the induced electric field originating from the out-of-plane electrical polarization of the Janus MoSSe layer, charge transfer between MoSSe and VS_2 layers and inter layer hybridization in Mo and V atom d_{z2} orbitals. We also established that the Interlayer charge transfer between MoSSe and VS_2 layers has largely reduced the required electric field to induce the half metallicity by shifting the electronic bands closer to the fermi level. Otherwise, inbuilt electrical polarization generated by Janus MoSSe layer becomes insufficient. This highlight that the external electric field which is required to induce half metallicity can be reduced by manipulating the charge transfer. These novel findings can be adopted to induce half metallic characteristics to many magnetic materials used in spintronic devices, and in the foreseeable future.

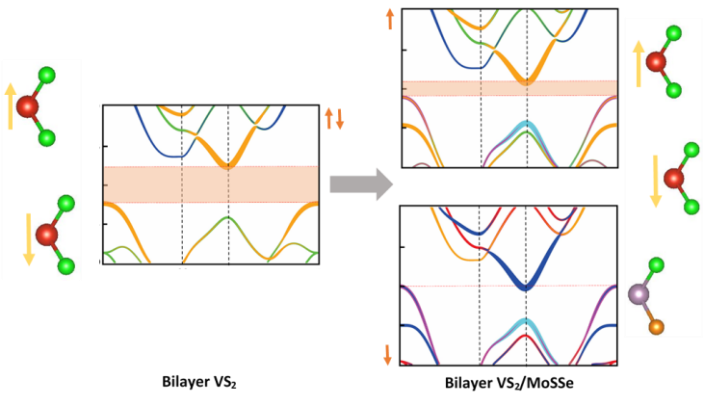

Keywords: VS_2, MoSSe, Half Metal, antiferromagnetic, ferromagnetic,2D materials

Introduction

Spintronics encompasses a broad range of technologies that aim to utilize the spin degree of freedom, in addition to the electrical charge, and perform memory and logic operations in electronic devices. It is identifying the ability to generate 100% spin-polarized that is currently a key asset for the performance of spintronic devices. Half-metallic materials can easily accomplish this task since their electronic structure sustains an electrical current composed of a single spin channel.[1-2] While, half-metallic properties have been identified in a broad range of compounds including perovskites[3], oxides[4], graphene nanoribbons[5], nitride mxenes[6], heusler alloys[7-8], transition-metal dinitrides[9] and graphitic carbon nitride[10], most known half metals are bulk materials, and the 2D structures that exhibit half-metallicity are a rarity. 2D half metals have recently taken some spotlights as promising spintronics media, due to the possibility of fine tuning their electrical, optical, mechanical and surface properties[11]. However, when thinned down to the bilayer, the majority of 2D magnetic compounds tend to exist in an antiferromagnetic (AFM) form[12-13] which means achieving half metallicity in such compounds remains challenging.

The complexity encountered in synthesizing the intrinsic 2D half metals predicted by theoretical studies has led researchers to explore novel strategies to induce half metallicity in existing 2D materials. Zhou *et al.* predicted ferromagnetism (FM) in layered NbS_2 and $NbSe_2$ under strain, with an half-metallic electronic structure appearing for biaxial strains in the region of 10%.[14] Li *et al.* showed that a free-standing $MnPSe_3$ nanosheet can be transformed into a half metal by carrier doping.[15] Gao *et al.* demonstrated, by using first-principles calculations, that point defect in a $CrCl_3$ single layer can cause an insulator to half-metal transition.[16] Kan *et al.* proposed that some morphological modifications, such as edge manipulation, can be a practical tool to induce half-metallicity in zigzag graphene ribbons.[17] An external electric field applied across a 2D layer can also induce half metallicity in graphene nano ribbons[5] and bilayer VSe_2.[18] These strategies of doping, morphological modifications, strain and defects engineering, all require precise control during the material synthesis, and so may be not practical. The application of an external electric field is also problematic, since the necessary fields are often enormous, typically more than can be achieved in a lab, and with the half metallic effect remaining volatile.

This research established that proximity with a Janus MoSSe monolayer can induce robust half metallicity in a bilayer VS_2. Bilayers VX_2 (X = S, Se and Te) exhibit a AFM type-1 magnetic ground

state[19], where ferromagnetic monolayers[20-22] are antiferromagnetically coupled to each other. Few layers/bilayers VX_2 were experimentally synthesised on several occasions,[23-27] with the extraction of monolayers challenging. Experimentally, Janus MoSSe has been successfully synthesized from chemical vapor deposition by replacing S with Se in as-grown MoS_2.[28-29] Here, the crystal asymmetry of 2D MoSSe induces a large out-of-plane electrical polarization and can be used as a source of electric-field to manipulate the electronic structure of a bilayer VX_2. This research presented here examined the magnetic and electronic properties of bilayer VS_2 and bilayer VS_2/MoSSe heterostructures (HTSs) by using first principles calculations. By identifying that the band structure of bilayer VS_2 changed from a semiconductor to a half-metal character in the presence of Janus MoSSe it can be suggested that the strategy of interfacing 2D magnetic materials with Janus monolayers may be a new weapon in the development of half-metallic antiferromagnets in low dimensions.

Computational Details

All calculations were carried out using Vienna Ab Initio Simulation Package (VASP) which uses density functional theory to solve the calculations.[30] The generalized gradient approximation (GGA) with the Perdew, Burke and Ernzerhof (PBE) parameterization of the exchange and correlation functional was used throughout,[31] together with the projector augmented-wave (PAW) method.[32-33] A vacuum region of 20Å was inserted in the cell to prevent interaction between the periodic images, while the cut-off energy was set to 500eV. The convergence criteria were $1x10^{-6}$ eV for the energy, and $1x10^{-3}$ eV/ Å for the Hellmann–Feynman forces. A gamma-centred 21 x 21 x 1 grid was used for all calculations since a dense k-point mesh is required for accurate total-energy predictions. The D3 scheme was employed to account for van der Waals interactions[34] and dipole corrections were included. The strongly correlated nature of VS_2 requires additional corrections, which were taken into account through the GGA+*U* scheme (PBE+*U*) introduced by Dudarev et al.[35] The Coulomb parameter, U_{eff} was set to the VS_2 accepted value of 3 eV[36] which was also calculated using a linear response method based on the magnetic ground state of the monolayers[37].

Results and Discussion

This theoretical simulation firstly established the possibility of having five different stacking configurations (see figure 1 top) based on the high symmetry points of atoms. Since each configuration can have either an FM or AFM alignment, our aim was to identify the ground

state configuration and its magnetic alignment (AFM/FM). The simulation results (Table 1) did establish that all configurations preferable to exist in the AFM state, with the AB stacking order the most stable among the five, and that AA' and AB' stacking configurations are very close to it in terms of energy. Since the AA' and AB' have only ~1-2 meV higher energy than the AB stacking order, those structures also have the potential of becoming the ground state under external stimuli. The calculated lattice constants of the relaxed AB-stacked VS_2 bilayer and MoSSe monolayer are 3.202Å and 3.23Å, respectively. Lattice mismatch between MoSSe and Bilayer VS_2 is 0.88% and is too small to impact the material properties.

***Table 1**:Total Energies of bilayer VS_2 in five different stacking orders (Figure 1), in corresponding FM and AFM magnetic State.*

Stacking Order	FM (eV)	AFM (eV)
AA	-34.790582	-34.791837
AA'	-34.840458	-34.842825
AC	-34.792024	-34.793854
AB	-34.843076	**-34.844153**
AB'	-34.841053	-34.843120

Having established that the bilayer VS_2 exhibits the lowest energies in AB, AB' and AA' stackings, the next step was to examine the stacking and magnetic order of the bilayer VS_2 and MoSSe heterostructure (HTS). In doing so we assumed that the bilayer VS_2 can only exist in one of those stacking configurations (AB, AB' and AA'). By keeping the bilayer VS_2 stacking order fixed, the position of MoSSe changed between the high symmetry points to obtain all possible stacking arrangements. Figure 1 illustrates the six stacking orders for the AB-stacked bilayer VS_2 and MoSSe HTS. The geometries can be constructed similarly for the AA' and AB' stackings. The stacking order, ABC4, appeared to be the ground state structure for the HTS (Table 2) with AFM magnetic alignment. Therefore, the ABC4 stacking order with AFM state was considered in all calculations.

Table 2: Total Energies of bilayer VS_2 /MoSSe heterostructures stacked in eighteen different arrangements. Six different stacking orders for AB-stacked bilayer VS_2 /MoSSe HTS are presented in figure 1.

Stacking Order		**AA'**	**AB**	**AB'**
C1	FM	-56.474203	-56.472853	-56.412229
	AFM	-56.476240	-56.473735	-56.414370

C2	FM	-56.477694	-56.476442	-56.474100
	AFM	-56.479825	-56.477315	-56.475990
C3	FM	-56.412062	-56.416474	-56.477866
	AFM	-56.414204	-56.417484	-56.479744
C4	FM	-56.474053	-56.480140	-56.414191
	AFM	-56.476267	**-56.481028**	-56.416252
C5	FM	-56.470193	-56.476274	-56.474249
	AFM	-56.472268	-56.477122	-56.476149
C6	FM	-56.414041	-56.415616	-56.470521
	AFM	-56.416190	-56.414605	-56.472402

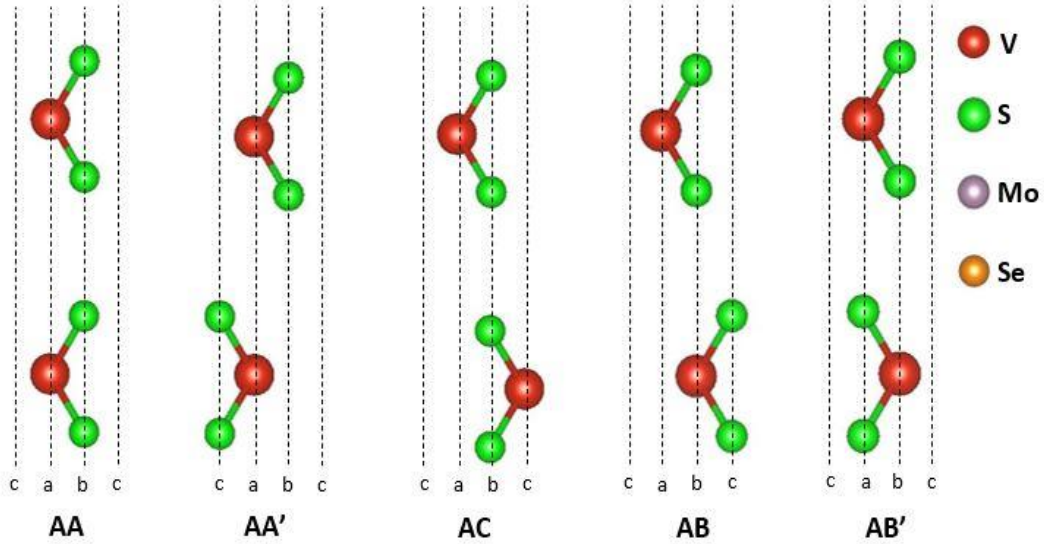

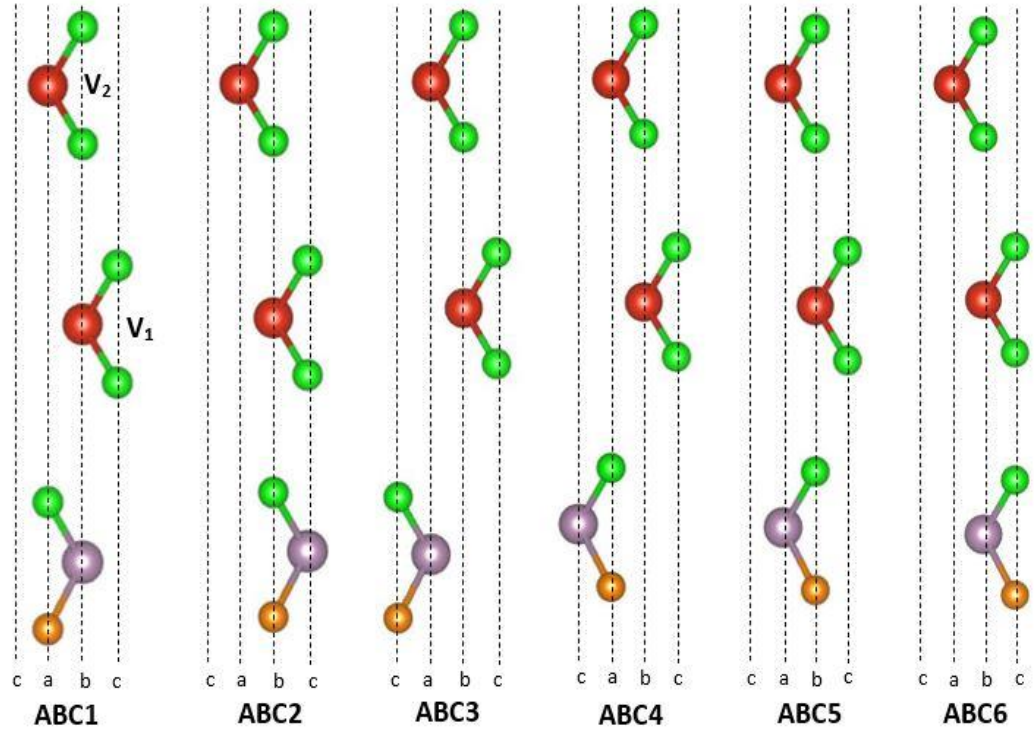

Figure 1: *Side views of bilayer VS_2 and bilayer VS_2/MoSSe heterostructure in different stacking arrangements. AA, AA', AC, AB and AB' are different stacking orders of bilayer VS_2.ABC1, ABC2, ABC3, ABC4, ABC5 and ABC6 are different stacking orders of AB-stacked bilayer VS_2 / MoSSe Heterostructure. Here V1 and V2 refers to top and bottom Vanadium atoms respectively.*

Table 3: *Bandgaps of bilayer VS_2 and monolayer MoSSe, calculated at the PBE/PBE+U level and compared with reference values obtained with PBE, HSE06 and experiments.*

	PBE+U/PBE (this work)	**PBE+U/PBE**	**HSE06**	**Experiment**
Bilayer 2H VS_2	~0.48eV	0.5 eV[36]	0.721 eV[38]	-
MoSSe	1.65 eV	1.56 eV[39]	2.09 eV[39]	1.68 eV[28]

The stability of the HTS is assessed by calculating the binding energy, E_b, through equation 1.

$$E_b = E_{tot} - E_{VS2} - E_{MoSSe} \quad (1)$$

Here, the total energies of the HTS, of the VS_2 bilayer and of the MoSSe layer are denoted as E_{tot}, E_{VS2} and E_{MoSSe}, respectively, with negative values of E_b indicating a stable HTS.

Table 4*: Calculated total energy, E_{tot}, binding energy, E_b, and net magnetic moment, μ_b, of Bilayer VS_2 and Bilayer VS_2/MoSSe heterostructures with AFM and FM magnetic configurations.*

	E_{tot} (eV)	E_{VS2} (eV)	E_{MoSSe} (eV)	E_b (eV)	μ_B
Bilayer VS_2 AFM	-34.844153	-34.844153	-	-	0.00
Bilayer VS_2 FM	-34.843076	-34.843076	-	-	2.00
BilayerVS_2/MoSSe AFM	-56.481028	-34.844153	-21.398196	-0.238679	0.00
Bilayer VS_2/MoSSe FM	-56.480140	-34.843076	-21.398196	-0.238679	2.00

Table 4 clearly demonstrates that the ground state of bilayer VS_2 is AFM and has an energy of 1.0meV lower than that of the FM configuration. The HTS formation also makes the AFM alignment more stable with an energy difference of 0.85meV compared with the FM. This energy difference reflects the proximity effect of the Janus MoSSe monolayer to the inter-layer exchange energy in the bilayer VS_2. The net magnetic moment in the FM VS_2 bilayer and bilayer VS_2/MoSSe HTS are 2.00 μB, with μB being the Bohr magneton.

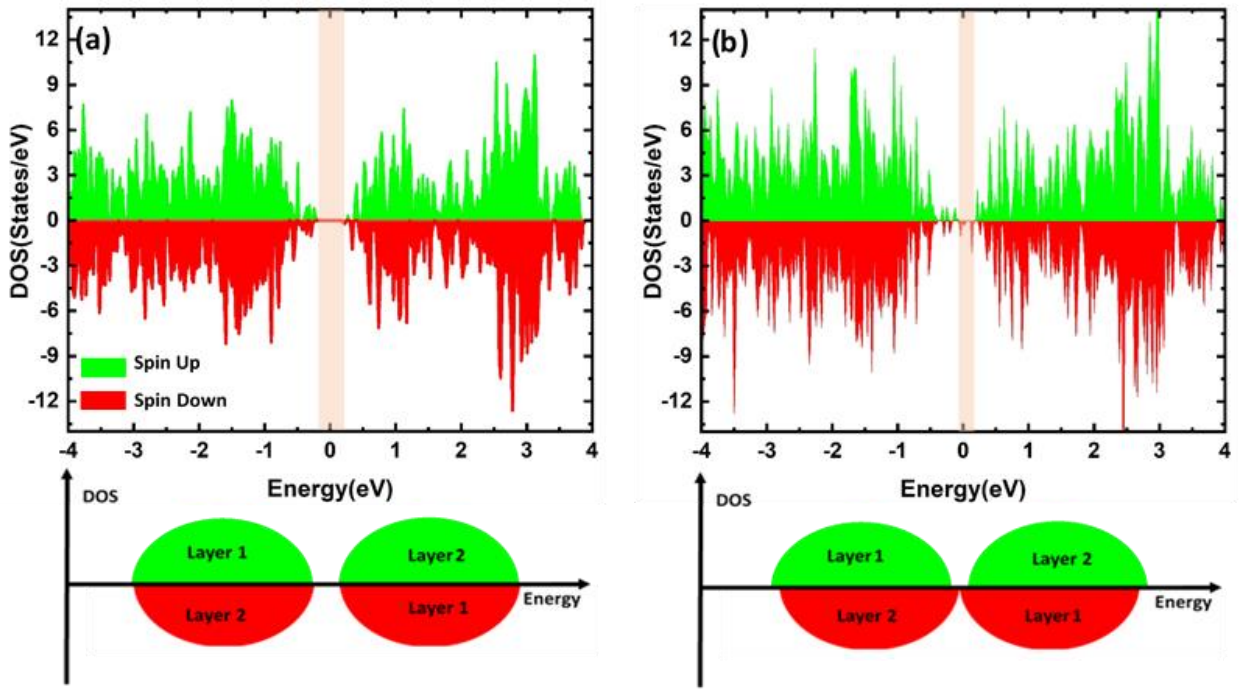

Figure 2 *: Total density of states of (a) the VS_2 bilayer and (b) the bilayer-VS_2/MoSSe HTS. The total spin up and spin down DOS are illustrated by green and red areas, respectively. The schematic representation of the spin-resolved density of states, separated by layer (layer1 /layer2), is also illustrated. Fermi level is located at zero.*

Further insight into the magnetic ground state and the interlayer alignment was established by looking at the PBE+*U* density of states (DOS) of Figure 2. DOS is shown for both the free-standing VS_2 bilayer [panel (a)] and HTS [panel (b)], together with the spin-resolved projections. In the case of VS_2, the individual monolayers appear to be ferromagnetic small-gap semiconductors, coupled antiferromagnetically to each other which means their layer-resolved DOSs are identical except for a spin rotation. When contacted with MoSSe, the magnetic layer alignment remains AFM. In addition to magnetic alignment, the relative energy shift of the bands associated with the two individual monolayers (with some band distortion) is induced by the built-in electric field of MoSSe.[5] This relative energy shift results in an overall half-metal ground state, where a finite DOS at the Fermi energy, E_F, is present only for the spin down channel.

The magnetic and electronic properties of VS_2 bilayer and HTS described above is also confirmed by the band structure diagrams (Figure 3). The band responsible for the magnetism is an hybrid made of the empty *S p* orbitals and the d_{z2} orbital of V, which has an exchange split (by about 1eV), as previously reported.[40] The conduction and valence bands of the AFM VS_2 bilayer are both spin and layer degenerate, where each layer is characterized by a valence band of one spin and a conduction band of the opposite spin. The bandgap of the VS_2 bilayer is about 0.48 eV. The

bandstructure of the HTS reflects that the induced half-metallicity is not entirely due to the built-in electric field of MoSSe and in fact, is a result of charge transfer, band hybridization and a built-in electric field. The difference in fermi levels in each layer is what causes the charge transfer in HTS and as a result, bands contributed by the bilayer VS_2 shifted downwards while bands contributing to MoSSe shifted upwards. This shift of bands results in Mo d_{z2} band to appear in the valence manifold closer to E_F. However, as reflected by the bandstructure diagram, the valance band not only comprises the Mo d_{z2} but also the V d_{z2} band, and therefore suggests that hybridization could exists between V and Mo d_{z2} orbitals. This interlayer hybridization between bilayer VS_2 and MoSSe can be clearly identified by observing the valence band minimum (VBM) near the Γ region in band diagram and in partial density of states (PDOS) graphs (Figure 3 (d)and (f)). Substantial overlapping of PDOS for Mo d_{z2} and V d_{z2} orbitals near the VBM and their similarity in shape provides further evidence for interlayer hybridization. Spin-down (minority) band crosses the Fermi level due to the inbuilt electric polarization, and the material presents a spin gap of about 0.183 eV. The smaller relative energy shift in spin up and spin down bands indicates that the in inbuilt electric field induced by MoSSe is weak. However, it's still become capable of inducing half-metallicity to the material with the assistance of charge transfer between the layers. One key phenomenon of charge transfer is the shifting of the bands closer to the Fermi level which enables even small electric fields to facilitate the bands to cross the Fermi level. The second phenomena of band hybridization enable the valance band to be affected by the spin polarization. If the Mo d_{z2} orbital is not hybridized with V d_{z2} orbitals, then the valence band will not change with the spin carriers, and consequently may not show the properties of a half metal.

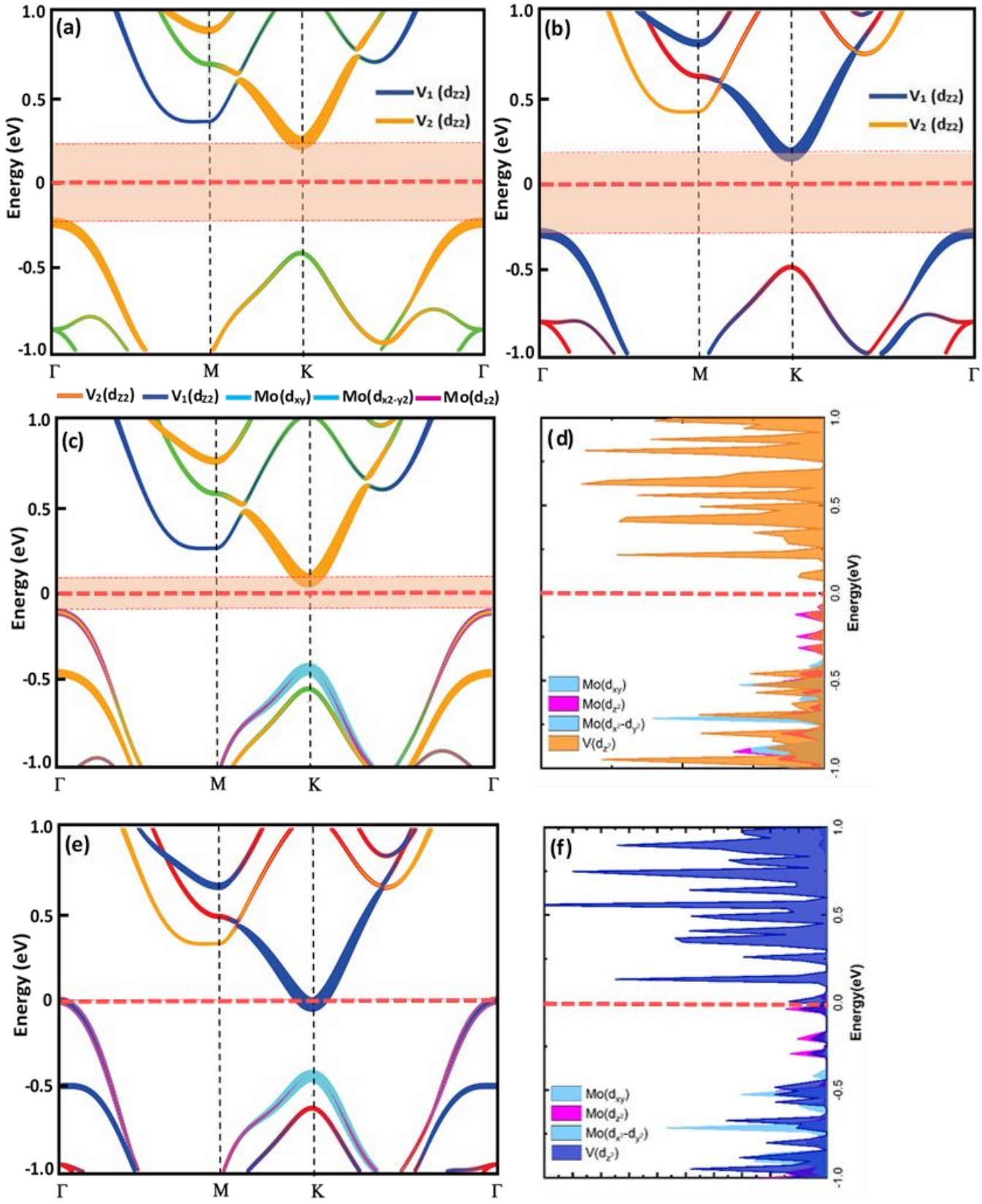

Figure 3: *Electronic band structure of (a) bilayer VS_2, spin up (b) bilayer VS_2, spin down and (c) MoSSe/bilayer-VS_2, spin up. (d) PDOS of MoSSe/bilayer-VS_2, spin up with each element orbitals are coloured, (e) Electronic band structure of MoSSe/bilayer-VS_2, spin down and (f) PDOS of MoSSe/bilayer-VS_2, spin down with each element orbitals are coloured. All calculated using PBE+U method. Apart from the colour codes illustrated in the graphs, rest of the spin*

up and spin down bands are indicated by green and red, respectively. Vanadium atom of layer 1 and layer 2 is denoted by V1 and V2, respectively. Orange, Navy blue, cyan and magenta colours indicate the contributions of d_{z2} orbital of V2, d_{z2} orbital of V1, d_{xy} and d_{x2-y2} orbital of Mo and d_{z2} orbital of Mo of the bands, respectively. Red dash line indicates the fermi level which is set to be zero.

The presence of the electrical polarization in the HTS has increased the charge redistribution, which was calculated by subtracting the charge density of the isolated MoSSe and VS_2 from that of the HTS (

Figure ***4*** (a)) where the charge depletion and accumulation are represented as cyan- and yellow-colored isosurfaces, respectively. Net charge is transferred from MoSSe to the bilayer VS_2 which agrees well with band offset in the bandstructure diagram (Figure 3). Bands created by the VS_2 have shifted downwards due to charge accumulation while bands created by the MoSSe have shifted upwards, owing to the charge depletion.

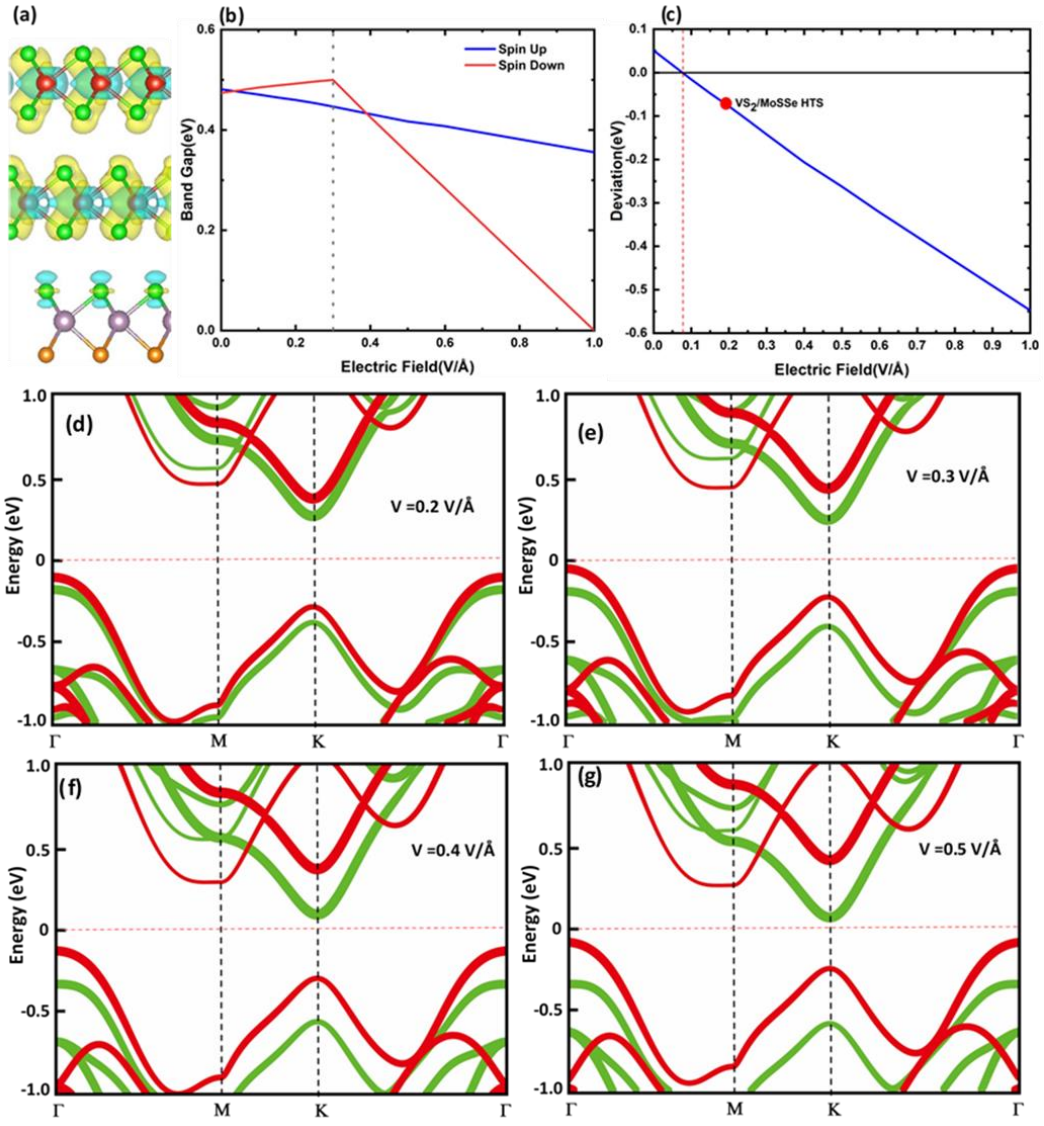

Figure 4*: Bilayer VS_2/MoSSe HTS (a) charge density redistribution. Charge accumulation and depletion indicated by yellow and cyan isosurfaces with value of 0.0003 e/ Å^3. (b) Spin-resolved band gap and (c) Deviation between the spin up and spin down valence band minimum, under an external electric field. Built in electric field 0.078 V/Å is marked by the red dash line. The large red dot indicates the value corresponding to the bilayer VS_2/MoSSe HTS. Bandstructure of bilayer VS_2 under external electric field of (d) 0.2 V/ Å (e) 0.3 V/ Å (f) 0.4 V/ Å and (g) 0.5 V/ Å. Spin up and spin down bands represented in green and red colours, respectively. Fermi level is set to zero.*

To establish a deeper understanding of the phenomena of inducing half metallicity to bilayer VS_2, variations in the bandstructure of the bilayer VS_2 under different external voltages were investigated.

Figure ***4***(b) illustrates the variations in bandgap of spin up and spin down channels corresponding to the external electric field. Here, values for electric fields above 0.6 V/Å were calculated by extrapolating the values obtained for voltages lower than 0.6 V/Å owing to the convergence difficulty in high electric fields. In the Figure 4(d)-(g), band structures of bilayer VS_2 under external electric fields of (V = 0.2,0.3,0.4 and 0.5 V/Å) were illustrated. According to the

Figure ***4***(b), the band gap in the spin up channel continuously decreases with the increasing electric field while the band gap in the spin down channel reached a maximum of 0.5 at 0.3 V/Å before reaching zero at 1.0 V/Å. Therefore, half metallic properties in the bilayer VS_2 can be induced by the external electric fields higher than 1.0 V/Å.

Figure ***4***(c) illustrates the deviation of the valence band minimum between spin up and spin down channels where the deviation between these bands becomes increasingly greater with the increasing electric field. It can be seen that in the bilayer VS_2, the band gap and bands of spin up and spin down channels have a slight deviation, even when the external electric field is zero, suggesting slight amount of inbuilt electrical polarization in bilayer VS_2. Earlier findings of Lui et al[36] also confirms that bilayer VS_2 has ferroelectric properties. Assuming there should be no deviation between the spin up and spin down bands when the external electric field is zero, we calculated the inbuilt electric field of the bilayer VS_2 to be 0.078 V/Å (

Figure ***4***(c)). Using the same assumption, an effective electric field generated by the MoSSe was calculated as being equivalent to 0.193 V/Å. Figure 4(d) shows the bandstructure of bilayer VS_2 under external electric field of 0.2 V/Å which is almost similar to the predicted polarization of MoSSe. Previous results in

Figure ***4***(b) showed that a minimum external electric field of 1.0 V/Å is required to induce half metallic properties to the bilayer VS_2, which means therefore, providing external electric field equal to the polarization generated by the MoSSe is not sufficient to make the material half metallic. The bandstructure diagrams of Figure 3, identify how the charge transfer and charge redistribution play a crucial role in shifting bands closer to the fermi level which enables half metallicity to be induced by a low electric field. An external electric field of 1.0 V/Å is extremely difficult to apply in laboratory conditions, which means such a strategy may not be practical to integrate into commonly used electronic devices. This research shows how the electric field that required to induce half metallicity can be drastically reduced by creating an interface with appropriate materials. Furthermore, that required external electric field can be fully eliminated by using an electrically polarized material such as MoSSe as an interface material.

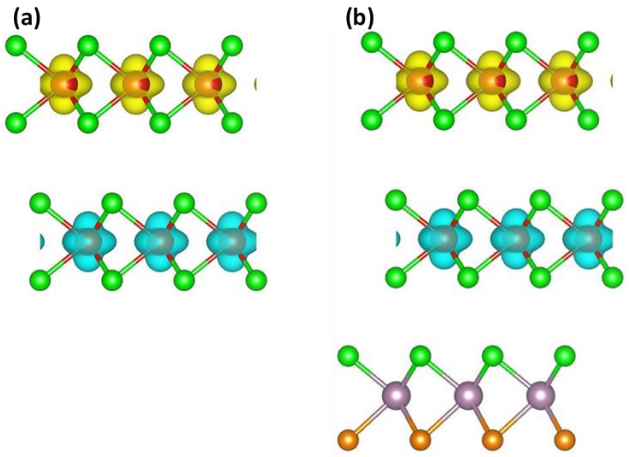

Figure 5: *Magnetism distributions (side views) of (a)bilayer VS_2 (b) bilayer VS2 and MoSSe HTS. The isosurface value was set to be 0.01 e/ Å^3. VASPKIT code was used to generate magnetic distributions.*[41]

Finally, we observe the magnetic distribution of bilayer VS_2 and Bilayer VS_2/MoSSe HTS as shown in the Figure 5. According to the figure, formation of the HTS doesn't does not have significant impact to magnetic distribution of the bilayer VS_2.This suggest that amount of interlayer charge transfer is not sufficient to affect the magnetic distribution of bilayer VS_2.

Conclusion

It is the use of first-principles calculations that identified a Janus MoSSe monolayer can be used to induce a half-metallic electronic structure for bilayer VS_2 while its ground-state remains in AFM alignment. Such an effect is driven mainly by the built-in electric field, originating from the intrinsic electrical polarization of MoSSe, as demonstrated by conducting explicit field-dependent calculations for a free-standing VS_2 bilayer. Apart from the inbuilt polarization of MoSSe, charge

transfer between the VS_2 bilayer and MoSSe helped significantly to induce half metallic properties. Explicit field-dependent calculations indicated that an electric field larger than 1.0 V/Å is required to induce half metallicity and such a high electric field is difficult to generate in a standard research laboratory. MoSSe has generated an effective electric field of 0.193 V/Å which is significantly less than the required external electric field of 1.0 V/A, and still capable of inducing the half metallicity. This suggests that the required external electric field, to induce half metallicity in magnetic materials can be reduced by creating an interface with the appropriate materials. At present, only a handful of 2D materials display half metallic properties. Which means exploring new materials with half metallicity or inducing half metallicity to existing magnetic materials is vital for the development of efficient spintronic devices. Our proposal to use polarized materials such as Janus MoSSe does provide a practical and scalable alternative avenue to induce half metallicity to materials and achieve high performing spintronic devices.

Acknowledgements

We acknowledge generous grants of high-performance computing resources provided by NCI National Facility and the Pawsey Supercomputing Centre through the National Computational Merit Allocation Scheme supported by the Australian Government and the Government of Western Australia. A. D. also greatly appreciates the financial support of the Australian Research Council under Discovery Project (DP170103598, DP210100721, and DP210100331). S.S acknowledge financial support from the Irish Research Council [IR- CLA/2019/127].

References

1. Awschalom, D. D.; Flatté, M. E., Challenges for semiconductor spintronics. *Nature Physics* **2007,** *3* (3), 153-159.
2. Coey, J. M. D.; Sanvito, S., Magnetic semiconductors and half-metals. *Journal of Physics D: Applied Physics* **2004,** *37* (7), 988-993.
3. Kato, H.; Okuda, T.; Okimoto, Y.; Tomioka, Y.; Oikawa, K.; Kamiyama, T.; Tokura, Y., Structural and electronic properties of the ordered double perovskites ${A}_{2}M{\mathrm{ReO}}_{6}$ $(A$=Sr,Ca; M=Mg,Sc,Cr,Mn,Fe,Co,Ni,Zn). *Physical Review B* **2004,** *69* (18), 184412.
4. Coey, J. M. D.; Venkatesan, M., Half-metallic ferromagnetism: Example of CrO2 (invited). *Journal of Applied Physics* **2002,** *91* (10), 8345-8350.
5. Son, Y.-W.; Cohen, M. L.; Louie, S. G., Half-metallic graphene nanoribbons. *Nature* **2006,** *444* (7117), 347-349.
6. Kumar, H.; Frey, N. C.; Dong, L.; Anasori, B.; Gogotsi, Y.; Shenoy, V. B., Tunable Magnetism and Transport Properties in Nitride MXenes. *ACS Nano* **2017,** *11* (8), 7648-7655.
7. Gao, G. Y.; Yao, K.-L., Antiferromagnetic half-metals, gapless half-metals, and spin gapless semiconductors: The D03-type Heusler alloys. *Applied Physics Letters* **2013,** *103* (23), 232409.
8. Chen, X.-Q.; Podloucky, R.; Rogl, P., Ab initio prediction of half-metallic properties for the ferromagnetic Heusler alloys Co2MSi (M=Ti,V,Cr). **2006,** *100* (11), 113901.

9. Wu, F.; Huang, C.; Wu, H.; Lee, C.; Deng, K.; Kan, E.; Jena, P., Atomically Thin Transition-Metal Dinitrides: High-Temperature Ferromagnetism and Half-Metallicity. *Nano Letters* **2015,** *15* (12), 8277-8281.
10. Du, A.; Sanvito, S.; Smith, S. C., First-Principles Prediction of Metal-Free Magnetism and Intrinsic Half-Metallicity in Graphitic Carbon Nitride. *Physical Review Letters* **2012,** *108* (19), 197207.
11. Novoselov, K. S.; Geim, A., The rise of graphene. *Nat. Mater* **2007,** *6* (3), 183-191.
12. Sun, Z.; Yi, Y.; Song, T.; Clark, G.; Huang, B.; Shan, Y.; Wu, S.; Huang, D.; Gao, C.; Chen, Z.; McGuire, M.; Cao, T.; Xiao, D.; Liu, W.-T.; Yao, W.; Xu, X.; Wu, S., Giant nonreciprocal second-harmonic generation from antiferromagnetic bilayer CrI3. *Nature* **2019,** *572* (7770), 497-501.
13. Hu, L.; Wu, X.; Yang, J., Mn2C monolayer: a 2D antiferromagnetic metal with high Néel temperature and large spin–orbit coupling. *Nanoscale* **2016,** *8* (26), 12939-12945.
14. Zhou, Y.; Wang, Z.; Yang, P.; Zu, X.; Yang, L.; Sun, X.; Gao, F., Tensile Strain Switched Ferromagnetism in Layered NbS2 and NbSe2. *ACS Nano* **2012,** *6* (11), 9727-9736.
15. Li, X.; Wu, X.; Yang, J., Half-Metallicity in MnPSe3 Exfoliated Nanosheet with Carrier Doping. *Journal of the American Chemical Society* **2014,** *136* (31), 11065-11069.
16. Gao, Y.; Wang, J.; Li, Y.; Xia, M.; Li, Z.; Gao, F., Point-Defect-Induced Half Metal in CrCl3 Monolayer. *physica status solidi (RRL) – Rapid Research Letters* **2018,** *12* (7), 1800105.
17. Kan, E.-j.; Li, Z.; Yang, J.; Hou, J. G., Half-Metallicity in Edge-Modified Zigzag Graphene Nanoribbons. *Journal of the American Chemical Society* **2008,** *130* (13), 4224-4225.
18. Gong, S.-J.; Gong, C.; Sun, Y.-Y.; Tong, W.-Y.; Duan, C.-G.; Chu, J.-H.; Zhang, X., Electrically induced 2D half-metallic antiferromagnets and spin field effect transistors. *Proceedings of the National Academy of Sciences* **2018,** *115* (34), 8511-8516.
19. Esters, M.; Hennig, R. G.; Johnson, D. C., Dynamic instabilities in strongly correlated ${\text{VSe}}_{2}$ monolayers and bilayers. *Physical Review B* **2017,** *96* (23), 235147.
20. Ma, Y.; Dai, Y.; Guo, M.; Niu, C.; Zhu, Y.; Huang, B., Evidence of the Existence of Magnetism in Pristine VX2 Monolayers (X = S, Se) and Their Strain-Induced Tunable Magnetic Properties. *ACS Nano* **2012,** *6* (2), 1695-1701.
21. Zhang, H.; Liu, L.-M.; Lau, W.-M., Dimension-dependent phase transition and magnetic properties of VS2. *Journal of Materials Chemistry A* **2013,** *1* (36), 10821-10828.
22. Xu, K.; Chen, P.; Li, X.; Wu, C.; Guo, Y.; Zhao, J.; Wu, X.; Xie, Y., Ultrathin Nanosheets of Vanadium Diselenide: A Metallic Two-Dimensional Material with Ferromagnetic Charge-Density-Wave Behavior. *Angewandte Chemie International Edition* **2013,** *52* (40), 10477-10481.
23. Gao, D.; Xue, Q.; Mao, X.; Wang, W.; Xu, Q.; Xue, D., Ferromagnetism in ultrathin VS2 nanosheets. *Journal of Materials Chemistry C* **2013,** *1* (37), 5909-5916.
24. Feng, J.; Sun, X.; Wu, C.; Peng, L.; Lin, C.; Hu, S.; Yang, J.; Xie, Y., Metallic Few-Layered VS2 Ultrathin Nanosheets: High Two-Dimensional Conductivity for In-Plane Supercapacitors. *Journal of the American Chemical Society* **2011,** *133* (44), 17832-17838.
25. Liu, Z.-L.; Wu, X.; Shao, Y.; Qi, J.; Cao, Y.; Huang, L.; Liu, C.; Wang, J.-O.; Zheng, Q.; Zhu, Z.-L.; Ibrahim, K.; Wang, Y.-L.; Gao, H.-J., Epitaxially grown monolayer VSe2: an air-stable magnetic two-dimensional material with low work function at edges. *Science Bulletin* **2018,** *63* (7), 419-425.
26. Yuan, J.; Wu, J.; Hardy, W. J.; Loya, P.; Lou, M.; Yang, Y.; Najmaei, S.; Jiang, M.; Qin, F.; Keyshar, K.; Ji, H.; Gao, W.; Bao, J.; Kono, J.; Natelson, D.; Ajayan, P. M.; Lou, J., Facile Synthesis of Single Crystal Vanadium Disulfide Nanosheets by Chemical Vapor Deposition for Efficient Hydrogen Evolution Reaction. *Advanced Materials* **2015,** *27* (37), 5605-5609.
27. Su, J.; Wang, M.; Li, Y.; Wang, F.; Chen, Q.; Luo, P.; Han, J.; Wang, S.; Li, H.; Zhai, T., Sub-Millimeter-Scale Monolayer p-Type H-Phase VS2. *Advanced Functional Materials* **2020,** *30* (17), 2000240.
28. Lu, A.-Y.; Zhu, H.; Xiao, J.; Chuu, C.-P.; Han, Y.; Chiu, M.-H.; Cheng, C.-C.; Yang, C.-W.; Wei, K.-H.; Yang, Y.; Wang, Y.; Sokaras, D.; Nordlund, D.; Yang, P.; Muller, D. A.; Chou, M.-Y.; Zhang, X.; Li, L.-J., Janus monolayers of transition metal dichalcogenides. *Nature Nanotechnology* **2017,** *12* (8), 744-749.
29. Zhang, J.; Jia, S.; Kholmanov, I.; Dong, L.; Er, D.; Chen, W.; Guo, H.; Jin, Z.; Shenoy, V. B.; Shi, L.; Lou, J., Janus Monolayer Transition-Metal Dichalcogenides. *ACS Nano* **2017,** *11* (8), 8192-8198.
30. Kresse, G.; Furthmüller, J., Efficient iterative schemes for ab initio total-energy calculations using a plane-wave basis set. *Physical Review B* **1996,** *54* (16), 11169-11186.

31. Perdew, J. P.; Burke, K.; Ernzerhof, M., Generalized Gradient Approximation Made Simple. *Physical Review Letters* **1996,** *77* (18), 3865-3868.
32. Kresse, G.; Joubert, D., From ultrasoft pseudopotentials to the projector augmented-wave method. *Physical Review B* **1999,** *59* (3), 1758-1775.
33. Blöchl, P. E., Projector augmented-wave method. *Physical Review B* **1994,** *50* (24), 17953-17979.
34. Grimme, S.; Antony, J.; Ehrlich, S.; Krieg, H., A consistent and accurate ab initio parametrization of density functional dispersion correction (DFT-D) for the 94 elements H-Pu. **2010,** *132* (15), 154104.
35. Dudarev, S. L.; Botton, G. A.; Savrasov, S. Y.; Humphreys, C. J.; Sutton, A. P., Electron-energy-loss spectra and the structural stability of nickel oxide: An LSDA+U study. *Physical Review B* **1998,** *57* (3), 1505-1509.
36. Liu, X.; Pyatakov, A. P.; Ren, W., Magnetoelectric Coupling in Multiferroic Bilayer ${\mathrm{VS}}_{2}$. *Physical Review Letters* **2020,** *125* (24), 247601.
37. Wang, C.; Zhou, X.; Zhou, L.; Pan, Y.; Lu, Z.-Y.; Wan, X.; Wang, X.; Ji, W., Bethe-Slater-curve-like behavior and interlayer spin-exchange coupling mechanisms in two-dimensional magnetic bilayers. *Physical Review B* **2020,** *102* (2), 020402.
38. Kan, M.; Wang, B.; Lee, Y. H.; Sun, Q., A density functional theory study of the tunable structure, magnetism and metal-insulator phase transition in VS2 monolayers induced by in-plane biaxial strain. *Nano Research* **2015,** *8* (4), 1348-1356.
39. Wen, Y.-N.; Xia, M.-G.; Zhang, S.-L., Bandgap engineering of Janus MoSSe monolayer implemented by Se vacancy. *Computational Materials Science* **2018,** *152*, 20-27.
40. Zhuang, H. L.; Hennig, R. G., Stability and magnetism of strongly correlated single-layer ${\mathrm{VS}}_{2}$. *Physical Review B* **2016,** *93* (5), 054429.
41. Wang, V.; Xu, N.; Liu, J.-C.; Tang, G.; Geng, W.-T., VASPKIT: A user-friendly interface facilitating high-throughput computing and analysis using VASP code. *Computer Physics Communications* **2021,** *267*, 108033.